Supplementary Information (SI) for Journal of Materials Chemistry A.
This journal is © The Royal Society of Chemistry 2026

Supporting Information for

Novel Ruddlesden-Popper double anti-perovskites $Mg_4AA'C$: first-principles screening and device simulation study for high-efficiency photovoltaic absorbers

Yuqi Zhang [a,b], Kai Li [a,b], Siyu Zhang [a,b], Yanzhao Liu [a,b] and Min Zhang,[a,b*]

[a] *College of Physics and Electronic Information, Inner Mongolia Normal University, Hohhot 010022, China.*

[b] *Inner Mongolia Key Laboratory of Applied Condensed Matter Physics, Hohhot 010022, China.*

E-mail: zhangm@imnu.edu.cn;

CALCULATION METHOD

Considering the interaction between optical phonons and electrons, the carrier mobility can be calculated using the method proposed by Feynman.[1] The carrier mobility is given by the following equation:

$$\mu = \frac{3\sqrt{\pi}e}{2c\pi\omega_{\mathrm{LO}}m^{*}\alpha}\frac{\sinh(\beta/2)}{\beta^{5/2}}\frac{\omega^{3}}{v^{3}}\frac{1}{K} \tag{S1}$$

Where ω_{LO} represents the longitudinal optical phonon frequency, m^{*} is the effective mass of the charge carrier. The electron-phonon coupling constant is denoted by α, while β, ω, and v represent temperature-dependent parameters. The variable K is determined by β, ω, and v and serves as the dependent variable. The minimum values of ω and v are computed using the minimization of the polariton free energy.

ω_{LO} represents an effective LO phonon frequency, determined from the following averaging relation:

$$\frac{W^{2}}{\omega_{\mathrm{LO}}}\coth\left(\frac{hc\omega_{\mathrm{LO}}}{2k_{B}T}\right) = \sum_{i=1}^{n}\frac{W_{i}^{2}}{\omega_{\mathrm{LO},i}}\coth\left(\frac{hc\omega_{\mathrm{LO},i}}{2k_{B}T}\right) \tag{S2}$$

W_{i} denotes the vibrational strength of the i-th LO phonon mode.

The macroscopic optical properties of materials are usually represented by the complex dielectric function:

$$\varepsilon(\omega)=\varepsilon_1(\omega)+i\varepsilon_2(\omega) \tag{S3}$$

In this equation, $\varepsilon_1(\omega)$ and $\varepsilon_2(\omega)$ represent the real and imaginary components of the complex dielectric function respectively, with ω denoting the frequency of photons. The dielectric function demonstrates a linear response to electromagnetic interactions and is closely associated with the band gap value E_g. The determination of $\varepsilon_2(\omega)$ can be achieved through momentum matrix elements as expressed below:

$$\varepsilon_2(\omega)=\frac{4\pi^2 e^2}{\Omega}\lim_{q\to 0}\frac{1}{q^2}\sum_{c,v,k}2\omega_k\delta(\varepsilon_{ck}-\varepsilon_{vk}-\omega)\times\left\langle u_{ck+e_\alpha q}\middle|u_{ck}\right\rangle\left\langle u_{ck+e_\beta q}\middle|u_{vk}\right\rangle^* \tag{S4}$$

The equation includes e_α and e_β, which represent unit vectors along the α and β directions, q representing the wave number of incident electromagnetic waves, Ω representing the volume of a crystal cell, and c and v respectively representing conduction band and valence band. The imaginary part $\varepsilon_2(\omega)$ of the complex dielectric function is obtained through integration of momentum matrix elements between unoccupied and occupied wave functions in the Brillouin zone, representing the energy required for the formation of an electric dipole moment. This quantity is directly proportional to the absorption spectrum and reflects optical transitions from valence band maximum (VBM) to conduction band minimum (CBM) at the threshold energy level. The peak value corresponds to the number of electrons undergoing transition. The larger the imaginary components of the complex dielectric function, the greater the extent of electronic excitation and the poorer the insulation performance of the system. In this case, there is a higher possibility for electrons to absorb photons, resulting in a larger number of electrons in an excited state and a higher probability of transition occurring. The real part $\varepsilon_1(\omega)$ of the dielectric function is derived from the imaginary part using the Kramers-Kronig transformation[2]:

$$\varepsilon_1(\omega)=1+\frac{2}{\pi}P\int_0^\infty\frac{\omega'\varepsilon_2(\omega')}{\omega'^2-\omega^2}\mathrm{d}\omega' \tag{S5}$$

In the equation, P represents the Cauchy principal value of the integral. The polarization behavior of materials can be comprehended through $\varepsilon_1(\omega)$, which is commonly employed to indicate the magnitude of charge polarization in response to an external electric field and reflects the material's intrinsic energy storage capability. A higher dielectric constant signifies a more pronounced affinity for charges. If the influence of lattice vibrations is neglected, the value at

zero frequency or zero energy limit is the static dielectric constant $\varepsilon(0)$. The presence of a higher static dielectric constant can enhance the occurrence of low-level charge defects, thereby reducing radiation recombination and exciton binding energy. Additionally, it signifies a decrease in long-range Coulomb attraction due to the screening effect on charged defects and impurities, resulting in reduced carrier recombination, scattering, and trapping.[3]

The absorption coefficient α is a crucial parameter for assessing the light-absorbing capability of materials, and its relationship with frequency ω within a specific range of photon energy can be determined using the subsequent formula:

$$\alpha(\omega) = \sqrt{2}\omega\left[\sqrt{\varepsilon_1^2(\omega) + \varepsilon_2^2(\omega)} - \varepsilon_1(\omega)\right]^{1/2} \tag{S6}$$

In principle, the maximum efficiency of a solar cell is determined by the universally recognized and classical Shockley-Queisser (SQ) limit.[4] The mathematical formulation is as follows:

$$\eta = \frac{p_m}{p_{in}} \tag{S7}$$

The variables P_m and P_{in} respectively denote the peak power density and the total incident power density of the solar energy spectrum in the given equation. Due to the reliance solely on the electronic band gap value of the material, estimation of maximum efficiency in this method is approximate. Building upon this, Liping Yu and Zunger developed the Spectroscopic Limited Maximum Efficiency (SLME) method for solar cells.[5,6] The calculation of power density P can be obtained by multiplying current density J with voltage V, as depicted in the following equation.

$$P = JV = \left\{J_{\mathrm{sc}} - J_0\left[\exp\left(\frac{eV}{k_B T}\right) - 1\right]\right\}V \tag{S8}$$

In the equation, J_{sc} and J_0 represent short circuit current density and reverse saturation current density, respectively. The calculation of J_{sc} and J_0 can be derived if the absorption coefficient $\alpha(E)$, AM1.5G solar spectrum I_{sun}, and blackbody spectrum $I_{\mathrm{bb}}(E,T)$ are known. The corresponding formula is as follows:

$$J_{\mathrm{sc}} = e\int_0^{\infty} \alpha(E) I_{\mathrm{sun}}(E)\mathrm{d}E \tag{S9}$$

$$J_0 = \frac{J_0^{\mathrm{r}}}{f_{\mathrm{r}}} = \frac{e\pi}{f_{\mathrm{r}}}\int_0^{\infty} \alpha(E) I_{\mathrm{bb}}(E,T)\,\mathrm{d}E \tag{S10}$$

In the equation, J_0^r and f_r respectively denote the radiation composite current density and radiation composite current fraction.

The open circuit voltage is the maximum output voltage of a solar cell under zero current (open circuit) conditions. The calculation formula is as follows:

$$V_{oc} = \frac{k_B T}{e} \ln\left(1 + \frac{J_{sc}}{J_0}\right) \tag{S11}$$

The fill factor (FF) reflects the ratio of the actual output power of the solar cell to the ideal power, and is an important parameter to characterize the performance of the solar cell. The greater the value, the higher the photoelectric conversion efficiency of the battery. The formula is as follows:

$$FF = \frac{V_m \times J_m}{V_{oc} \times J_{sc}} \tag{S12}$$

In the equation, V_m and J_m represent the voltage and current density at the maximum power point (MPP), respectively.

In the devices simulation, we considered the model of narrowed bandgap. The Fermi-Dirac statistical theory was adopted to describe the distribution of charge carriers, and the Boltzmann approximation was abandoned. The transport characteristics of charge carriers under high carrier concentration and degeneracy conditions were accurately described. Simultaneous introduction of SRH defect recombination, Auger recombination and radiative recombination models in both the $Mg_4AA'C$ absorption layer and the TiO_2 electron transport layer corresponds to non-radiative recombination induced by intrinsic defect energy levels, Auger recombination under high carrier concentration, and band-to-band radiative recombination, respectively. At the $Mg_4AA'C/TiO_2$ interface, the interface SRH recombination model is adopted, considering carrier recombination loss caused by interface defect states. Optical simulation uses AM1.5G standard solar spectrum incidence, based on the transfer matrix method (TMM) to solve the light field distribution of multi-layer films, considering the standing wave effect caused by film optical interference and the wavelength dispersion characteristics of material refractive index and absorption coefficient. Electrical transport uses Poisson's equation coupled with the continuity equations of electrons and holes and the drift-diffusion equations to self-consistently solve, fully describing the internal potential distribution, carrier drift-diffusion and recombination dynamics processes in the device.

Table S1 Lattice constant and angle of double anti-perovskites $Mg_4AA'C$ (A = As, Sb, Bi; A' = Cl, Br, I).

Materials	a (Å)	b (Å)	c (Å)	$\alpha = \beta = \gamma$
Mg_4AsClC	4.287	4.287	14.019	90°
Mg_4AsBrC	4.320	4.320	14.197	90°
Mg_4AsIC	4.383	4.383	14.539	90°
Mg_4SbClC	4.367	4.367	14.564	90°
Mg_4SbBrC	4.394	4.394	14.763	90°
Mg_4SbIC	4.447	4.447	15.090	90°
Mg_4BiClC	4.398	4.398	14.732	90°
Mg_4BiIC	4.471	4.471	15.300	90°

Table S2 75 semiconductor materials identified from high-throughput screening of RP-type double anti-perovskites, together with their band gap types and PBE band gap values.

Materials	Type	E_g (eV)	Materials	Type	E_g (eV)	Materials	Type	E_g (eV)
Be_4NFC	Indirect	2.78	Mg_4PIC	Direct	0.36	Ca_4SbFSi	Direct	0.32
Be_4NClC	Direct	1.96	Mg_4AsFC	Direct	0.83	Ca_4SbFGe	Direct	0.23
Be_4NBrC	Direct	1.26	Mg_4AsFSi	Direct	0.35	Ca_4SbFSn	Indirect	0.12
Be_4PFC	Indirect	1.91	Mg_4AsFGe	Direct	0.18	Ca_4SbClC	Direct	0.11
Be_4PClC	Direct	0.66	Mg_4AsClC	Direct	0.97	$Ca_4SbClSi$	Direct	0.25
Be_4PBrC	Direct	0.25	$Mg_4AsClSi$	Direct	0.19	$Ca_4SbClGe$	Direct	0.17
Be_4AsFC	Indirect	1.69	$Mg_4AsClGe$	Direct	0.16	$Ca_4SbClSn$	Direct	0.15
Be_4AsClC	Direct	0.57	Mg_4AsBrC	Direct	0.78	Ca_4SbBrC	Direct	0.04
Be_4AsBrC	Direct	0.16	$Mg_4AsBrSi$	Direct	0.03	$Ca_4SbBrSi$	Direct	0.17
Be_4SbFC	Indirect	0.81	Mg_4AsIC	Direct	0.25	$Ca_4SbBrGe$	Direct	0.09
Be_4SbISn	Indirect	0.15	Mg_4SbFC	Indirect	0.80	$Ca_4SbBrSn$	Direct	0.12
Be_4BiFC	Indirect	0.33	Mg_4SbFSi	Indirect	0.25	Ca_4SbIC	Direct	0.08
Mg_4NFC	Direct	0.13	Mg_4SbFGe	Indirect	0.23	Ca_4SbISi	Direct	0.20
Mg_4NClC	Direct	0.36	Mg_4SbClC	Direct	0.67	Ca_4SbIGe	Direct	0.12
Mg_4NBrC	Direct	0.26	$Mg_4SbClSi$	Direct	0.09	Ca_4SbISn	Direct	0.15
Mg_4NIC	Direct	0.37	$Mg_4SbClGe$	Direct	0.06	Ca_4BiFC	Direct	0.08

Mg_4PFC	Direct	1.14	Mg_4SbBrC	Direct	0.40	Ca_4BiFSi	Direct	0.15
Mg_4PFSi	Direct	0.40	Mg_4BiFC	Indirect	0.17	Ca_4BiFGe	Direct	0.05
Mg_4PFGe	Direct	0.23	Mg_4BiFSi	Indirect	0.22	$Ca_4BiClSi$	Direct	0.06
Mg_4PClC	Direct	1.25	Mg_4BiFGe	Indirect	0.17	$Ca_4BiClSn$	Direct	0.01
Mg_4PClSi	Direct	0.22	Mg_4BiClC	Direct	0.37	Ca_4BiIC	Direct	0.08
Mg_4PClGe	Direct	0.19	$Mg_4BiClSi$	Direct	0.07	Zn_4NFC	Indirect	1.01
Mg_4PBrC	Direct	0.91	$Mg_4BiClGe$	Direct	0.05	Zn_4NClC	Direct	0.94
Mg_4PBrSi	Direct	0.05	Mg_4BiBrC	Direct	0.23	Zn_4NBrC	Direct	0.64
Mg_4PBrGe	Direct	0.01	Ca_4SbFC	Indirect	0.23	Zn_4NIC	Direct	0.04

Table S3 The J_{sc} (A/m^2), V_{oc} (V) and PCE (%) with thickness (μm) of $Mg_4AA'C$.

Materials	Mg_4AsClC			Mg_4AsBrC			Mg_4AsIC			Mg_4SbClC		
Thickness	J_{sc}	V_{oc}	PCE	J_{sc}	V_{oc}	PCE	J_{sc}	V_{oc}	PCE	J_{sc}	V_{oc}	PCE
0.5	1.59	50.12	7.30	1.32	102.71	12.22	0.75	277.87	17.87	1.18	127.24	13.50
1	1.58	66.40	9.60	1.30	127.72	15.04	0.74	326.17	20.55	1.17	155.39	16.30
2	1.56	83.96	12.04	1.29	152.16	17.73	0.73	365.56	22.51	1.16	184.32	19.09
4	1.55	103.35	14.70	1.28	177.59	20.45	0.71	400.23	24.05	1.14	215.21	22.00
8	1.54	123.81	17.44	1.26	203.66	23.17	0.69	432.59	25.35	1.13	246.11	24.82
15	1.53	141.65	19.78	1.25	225.80	25.40	0.68	459.19	26.30	1.11	271.71	27.05
30	1.51	159.01	21.99	1.24	246.69	27.39	0.67	483.26	26.97	1.10	295.61	29.00
50	1.50	169.84	23.31	1.22	259.38	28.53	0.65	497.29	27.23	1.09	310.10	30.10
100	1.49	181.83	24.70	1.21	273.22	29.68	0.64	511.14	27.31	1.08	325.67	31.17
200	1.47	191.02	25.70	1.20	283.79	30.46	0.63	518.41	27.07	1.06	337.04	31.82
300	1.47	195.30	26.14	1.19	288.68	30.79	0.62	520.26	26.83	1.06	314.98	32.06
Materials	Mg_4SbBrC			Mg_4SbIC			Mg_4BiClC			Mg_4BiIC		
Thickness	J_{sc}	V_{oc}	PCE	J_{sc}	V_{oc}	PCE	J_{sc}	V_{oc}	PCE	J_{sc}	V_{oc}	PCE
0.5	0.90	241.18	18.92	0.39	517.91	15.57	0.88	322.19	24.72	0.22	629.72	9.37
1	0.89	280.67	21.64	0.38	568.87	16.31	0.87	360.96	27.18	0.21	653.65	8.82
2	0.87	314.41	23.79	0.36	596.98	16.24	0.85	384.96	28.40	0.19	664.46	8.07
4	0.86	345.88	25.66	0.35	614.96	15.83	0.84	404.22	29.12	0.18	669.50	7.27
8	0.84	375.11	27.28	0.33	627.12	15.27	0.82	422.00	29.88	0.16	672.09	6.52

15	0.83	398.68	28.45	0.32	636.90	14.76	0.81	435.18	30.26	0.15	674.57	5.93
30	0.81	420.82	29.42	0.31	647.74	14.26	0.79	445.53	30.41	0.14	677.84	5.37
50	0.80	433.94	29.89	0.30	654.60	13.92	0.79	450.95	30.39	0.13	680.43	5.04
100	0.79	446.69	30.18	0.29	661.23	13.47	0.78	456.97	30.33	0.12	683.80	4.66
200	0.78	455.16	30.20	0.28	665.02	13.07	0.77	462.49	30.30	0.12	686.52	4.38
300	0.77	459.23	30.20	0.27	666.28	12.85	0.76	465.40	30.31	0.11	687.67	4.26

Table S4 The input parameters of Sentaurus TCAD simulations for $Mg_4AA'C$ soler cells.

Materials	Thickness (μm)	N_A (cm^{-3})	E_g (eV)	Affinity (eV)	$\varepsilon(0)$	N_c (cm^{-3})	N_v (cm^{-3})	μ_e ($cm^2 \cdot V^{-1} \cdot s^{-1}$)	μ_h ($cm^2 \cdot V^{-1} \cdot s^{-1}$)
TiO_2	0.04	1e18	3.20	4.00	86.00	1.00e20	1.00e19	0.1	0.01
$MAPbI_3$	0.4	-1e17	1.55	4.10	30.00	3.00e18	4.00e18	24	164
Mg_4AsClC	7.00	-1e17	1.65	0.69	19.28	2.05e18	7.47e19	800.59	19.63
Mg_4AsBrC	7.00	-1e17	1.35	1.02	50.76	3.91e18	4.18e19	118.08	9.02
Mg_4AsIC	7.00	-1e17	0.73	1.64	71.15	3.30e18	2.30e19	155.10	19.64
Mg_4SbClC	7.00	-1e17	1.14	1.25	18.61	5.00e18	8.02e19	197.15	10.75
Mg_4SbBrC	7.00	-1e17	0.85	1.55	50.90	4.33e18	4.69e19	128.19	9.78
Mg_4BiClC	7.00	-1e17	0.62	1.43	22.82	1.45e18	9.93e19	880.96	11.12

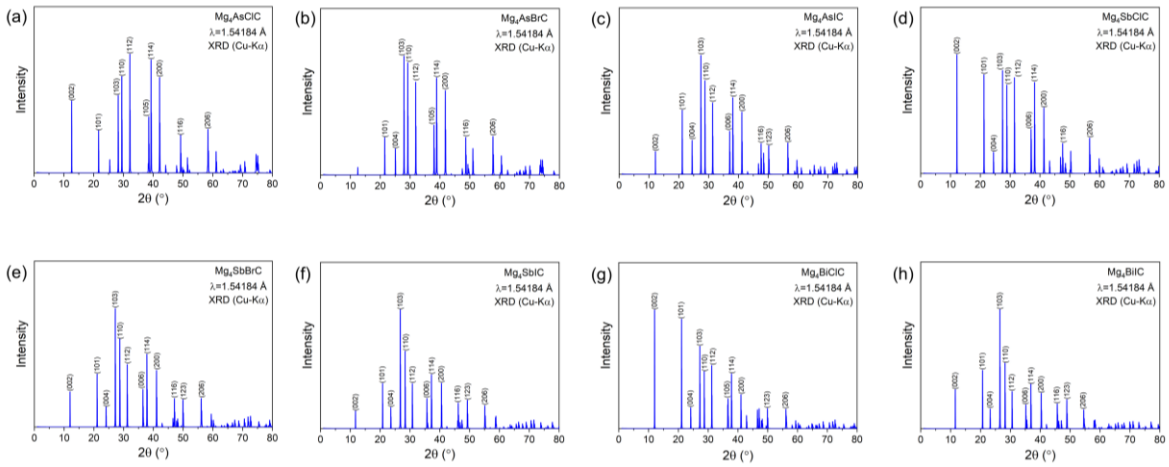

Fig.S1 X-ray diffraction (XRD) patterns of $Mg_4AA'C$ (A = As, Sb, Bi; A' = Cl, Br, I)

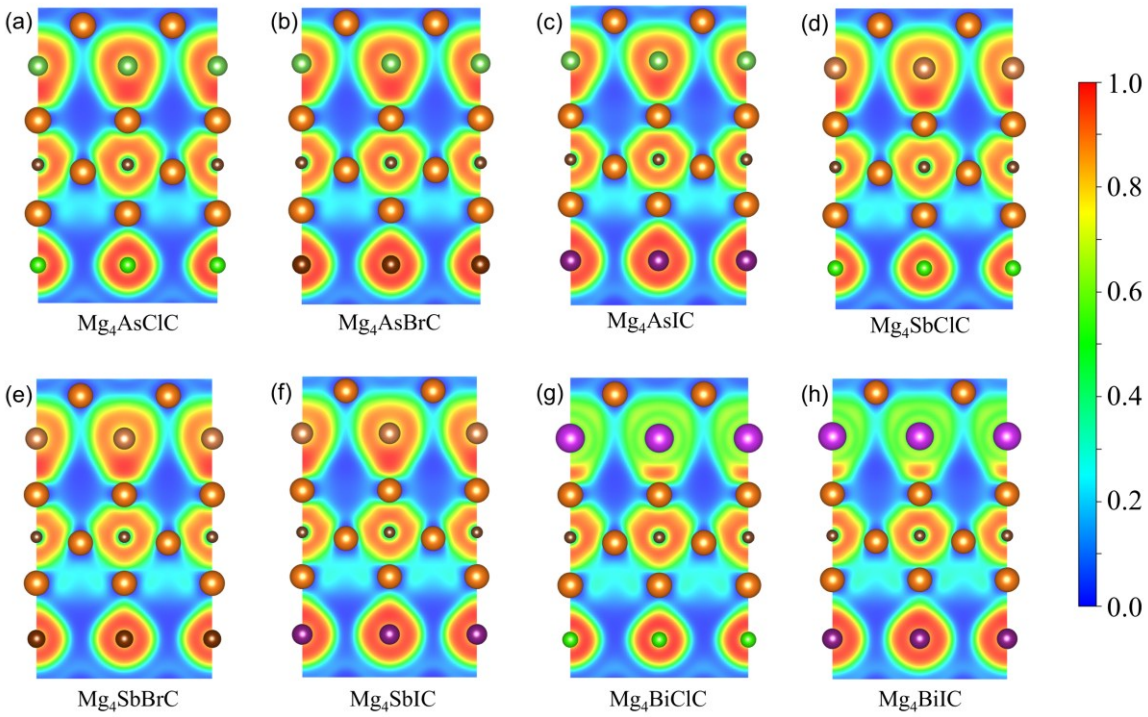

Fig.S2 Electron localization functions (ELF) in the (100) direction of $Mg_4AA'C$ (A = As, Sb, Bi; A' = Cl, Br, I)

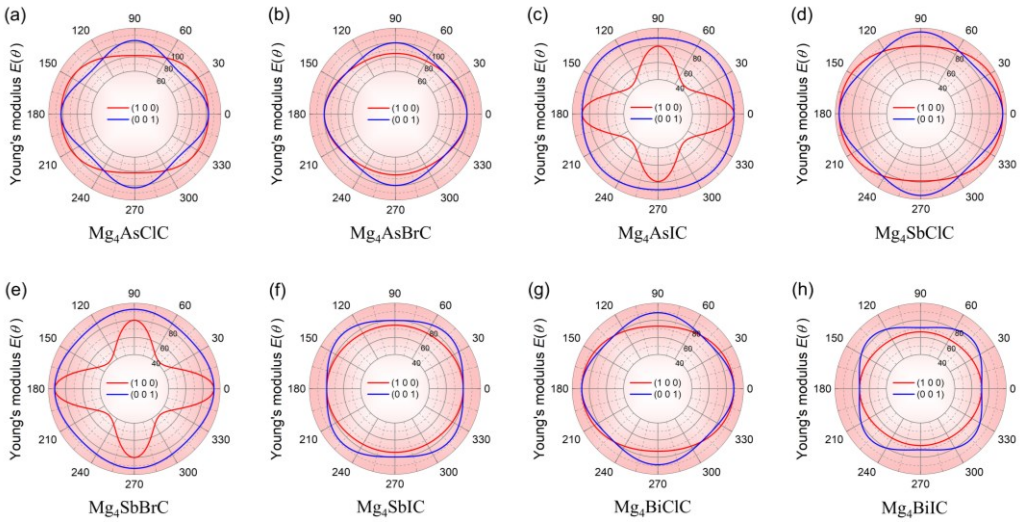

Fig.S3 The orientation-dependence of Young's modulus $E(\theta)$ of $Mg_4AA'C$ (A = As, Sb, Bi; A' = Cl, Br, I)

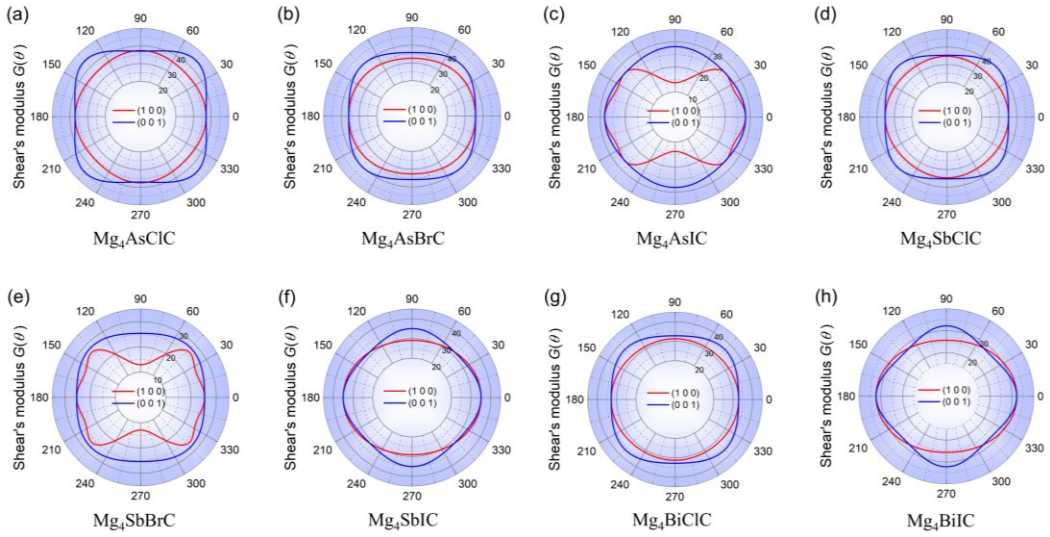

Fig.S4 The orientation-dependence of shear's modulus $G(\theta)$ of $Mg_4AA'C$ (A = As, Sb, Bi; A' = Cl, Br, I)

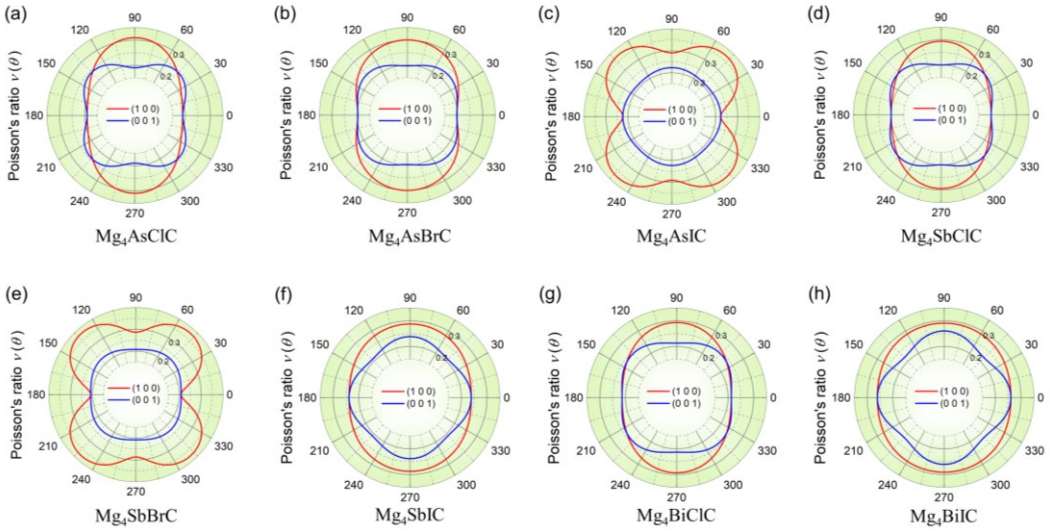

Fig.S5 The orientation-dependence of Poisson's ratio $v(\theta)$ of $Mg_4AA'C$ (A = As, Sb, Bi; A' = Cl, Br, I)

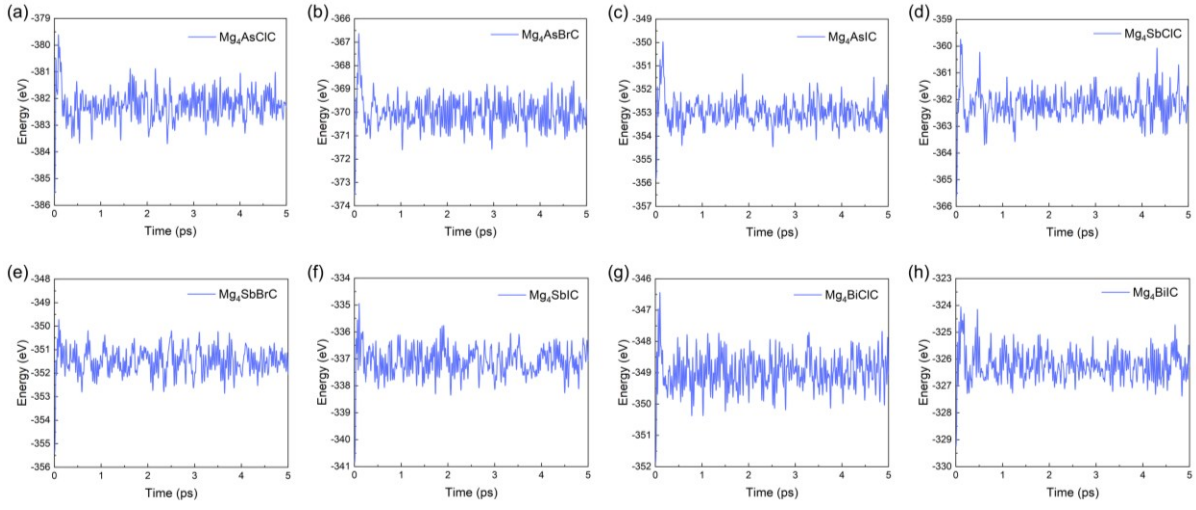

Fig.S6 *Ab initio* molecular dynamic (AIMD) simulation of $Mg_4AA'C$ (A = As, Sb, Bi; A' = Cl, Br, I)

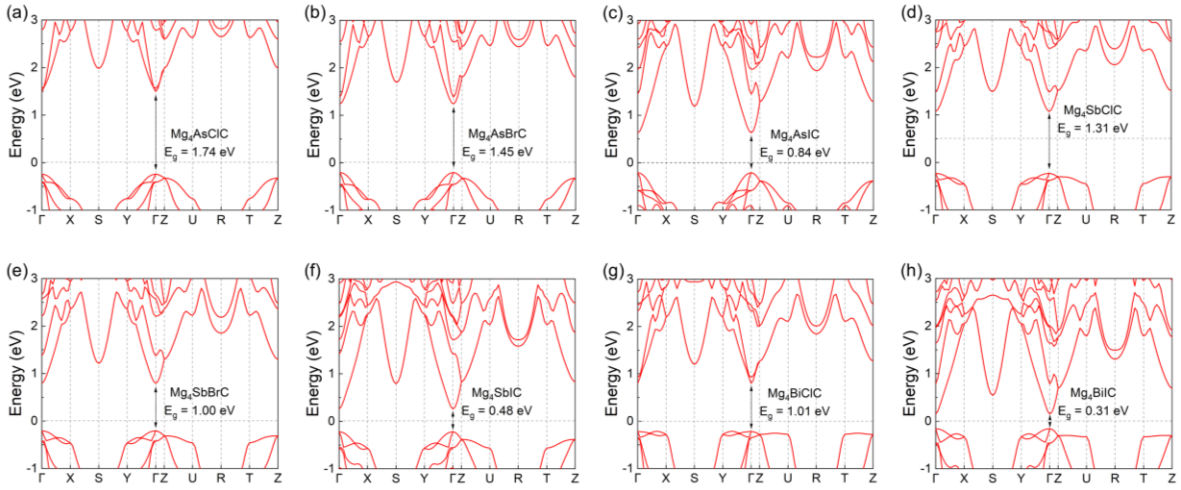

Fig.S7 HSE06 band structure of $Mg_4AA'C$ (A = As, Sb, Bi; A' = Cl, Br, I)

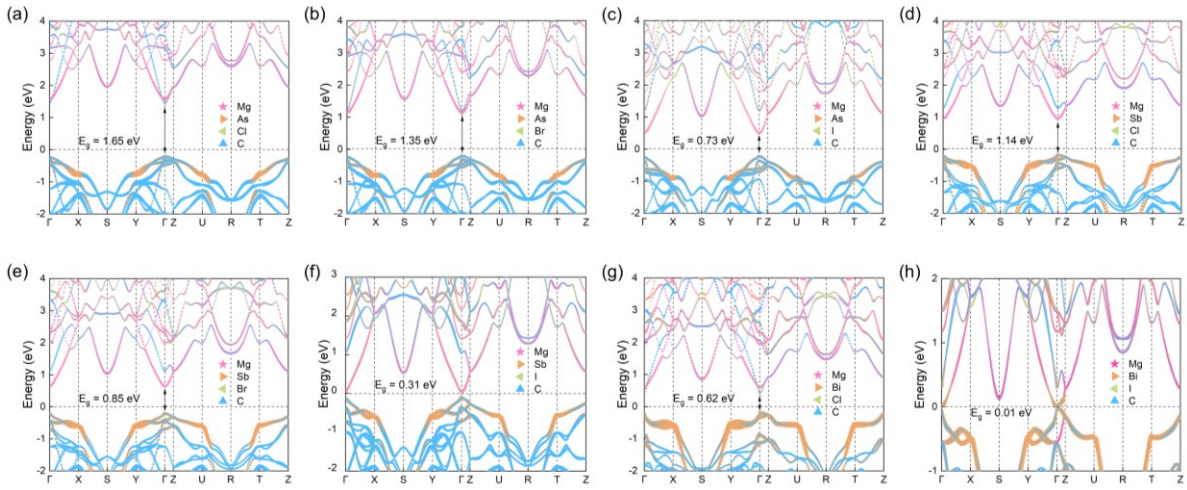

Fig.S8 HSE06+SOC projected band structure of $Mg_4AA'C$

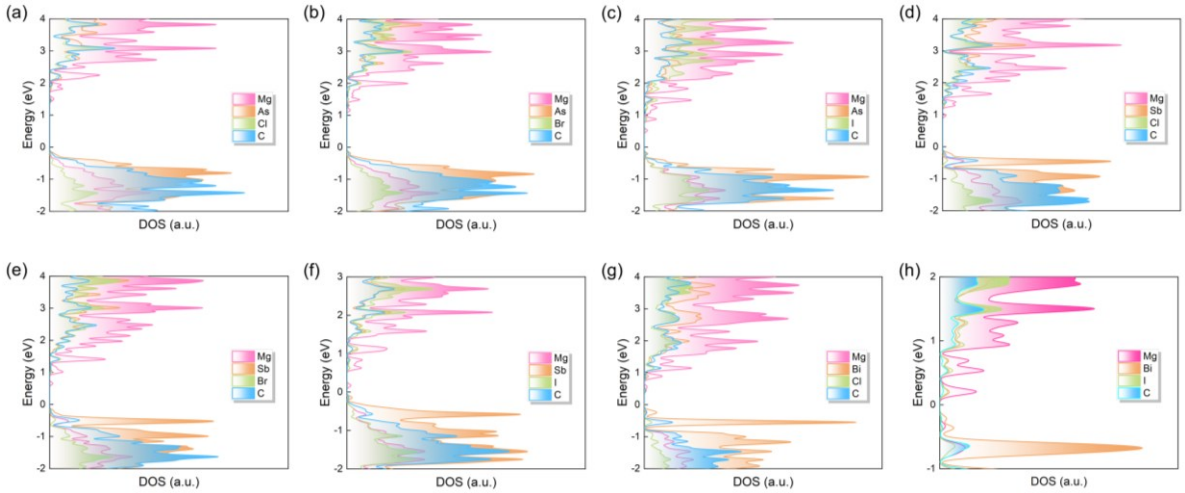

Fig.S9 Density of states of $Mg_4AA'C$ (A = As, Sb, Bi; A' = Cl, Br, I)

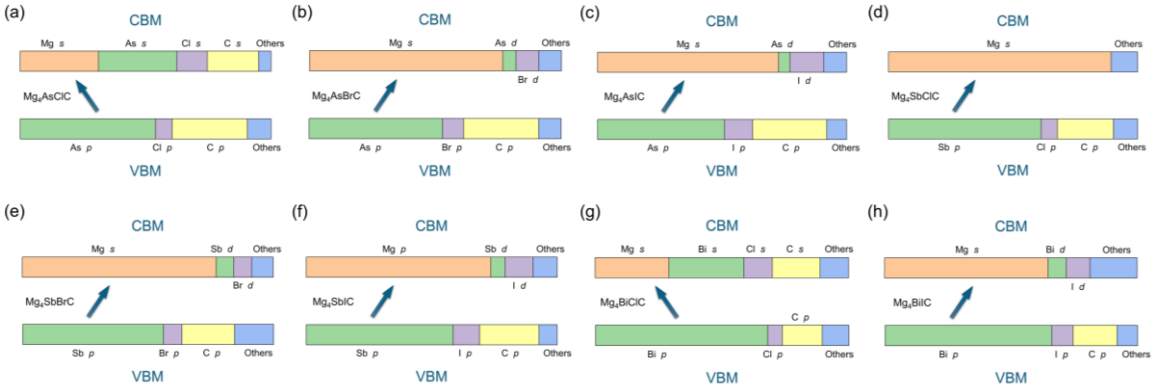

Fig.S10 Schematic illustration of orbital characters of VBM and CBM of $Mg_4AA'C$

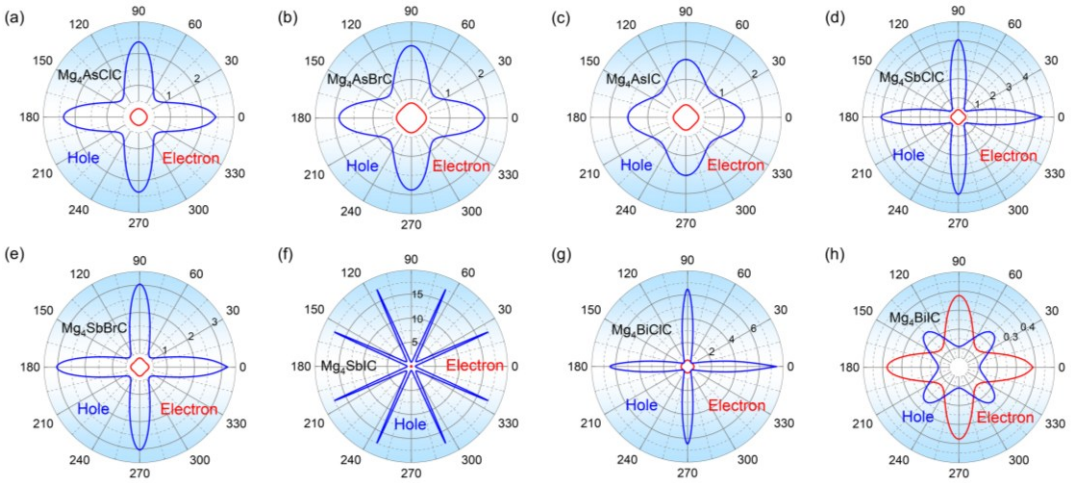

Fig.S11 Orientation-dependent carrier effective mass of $Mg_4AA'C$ (A = As, Sb, Bi; A' = Cl, Br, I)

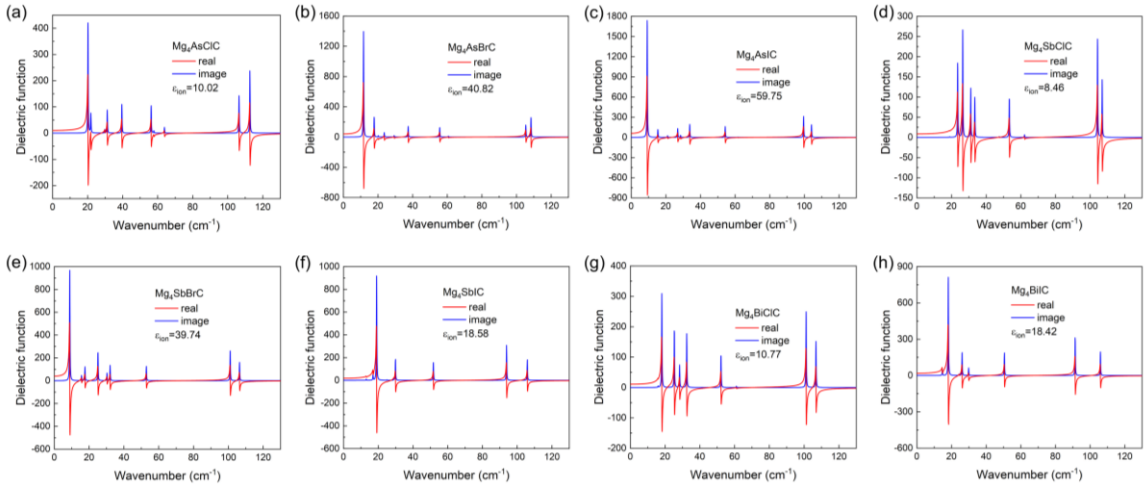

Fig.S12 Contributions of ions to the real and imaginary parts of dielectric functions of $Mg_4AA'C$ (A = As, Sb, Bi; A' = Cl, Br, I)

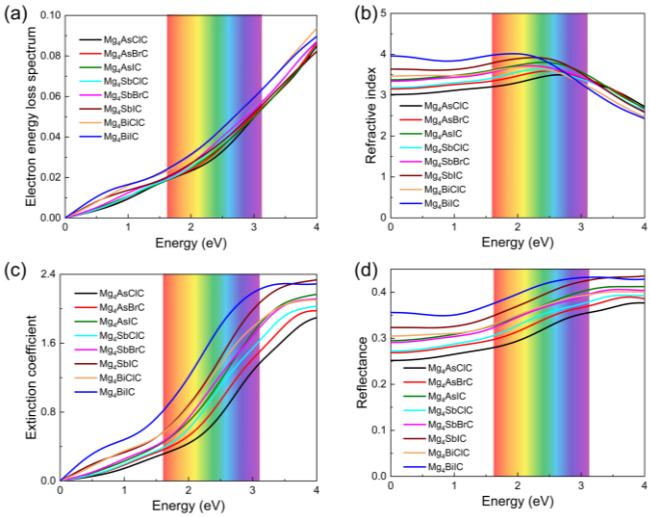

Fig.S13 Calculated optical properties of $Mg_4AA'C$: (a) electron energy-loss spectrum, (b) refractive index, (c) extinction coefficient, and (d) reflectance.

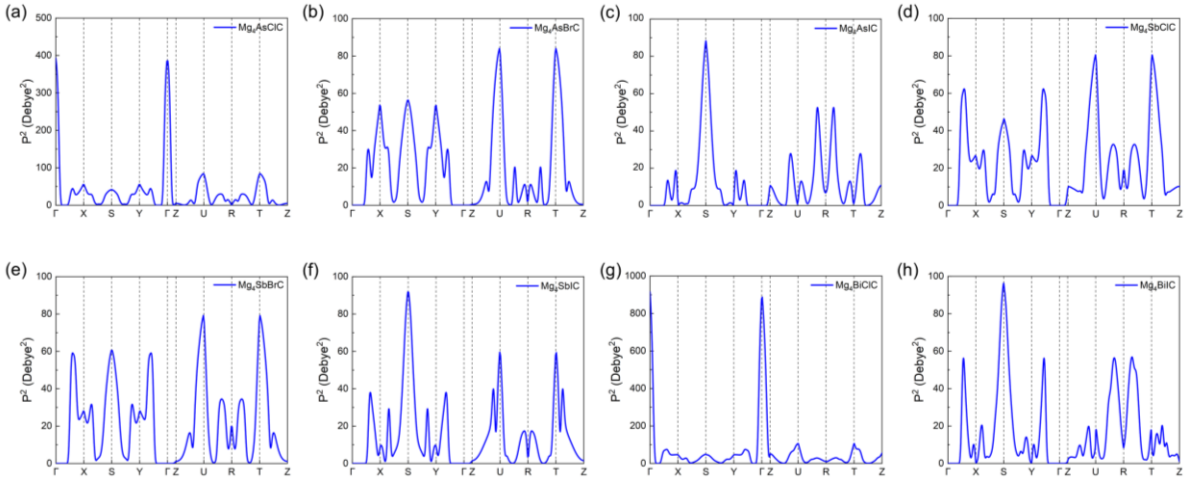

Fig.S14 Transition dipole moment of $Mg_4AA'C$ (A = As, Sb, Bi; A' = Cl, Br, I)

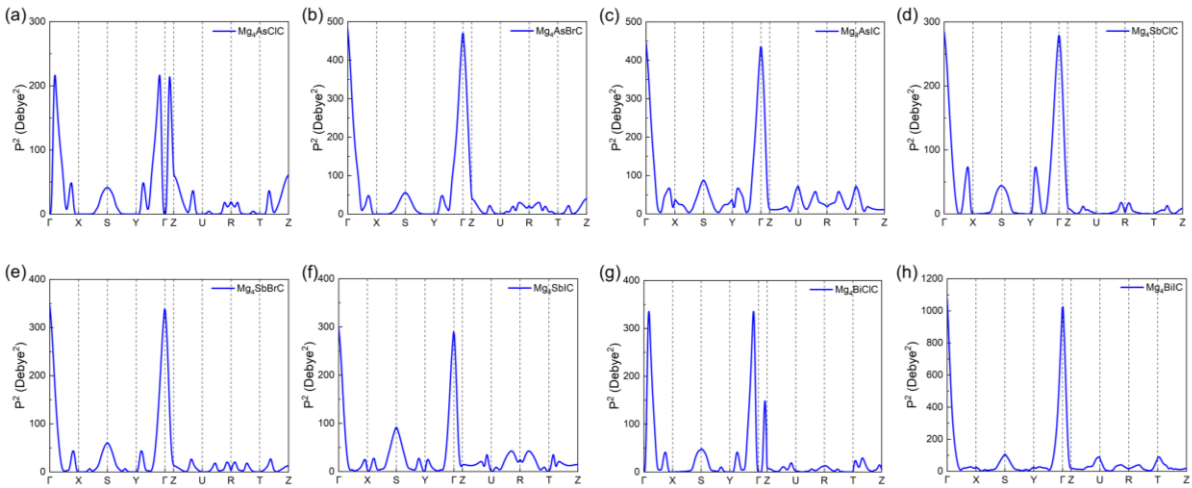

Fig.S15 Transition dipole moment of $Mg_4AA'C$ (A = As, Sb, Bi; A' = Cl, Br, I)

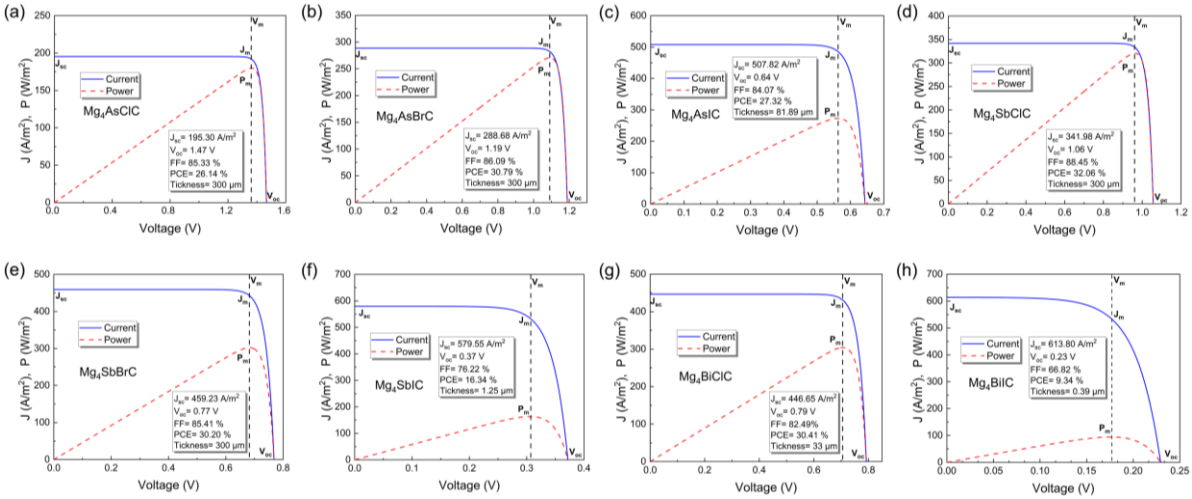

Fig.S16 Calculated *J-V* characteristic curve of $Mg_4AA'C$ (A = As, Sb, Bi; A' = Cl, Br, I) under AM1.5G solar illumination using the SLME model.

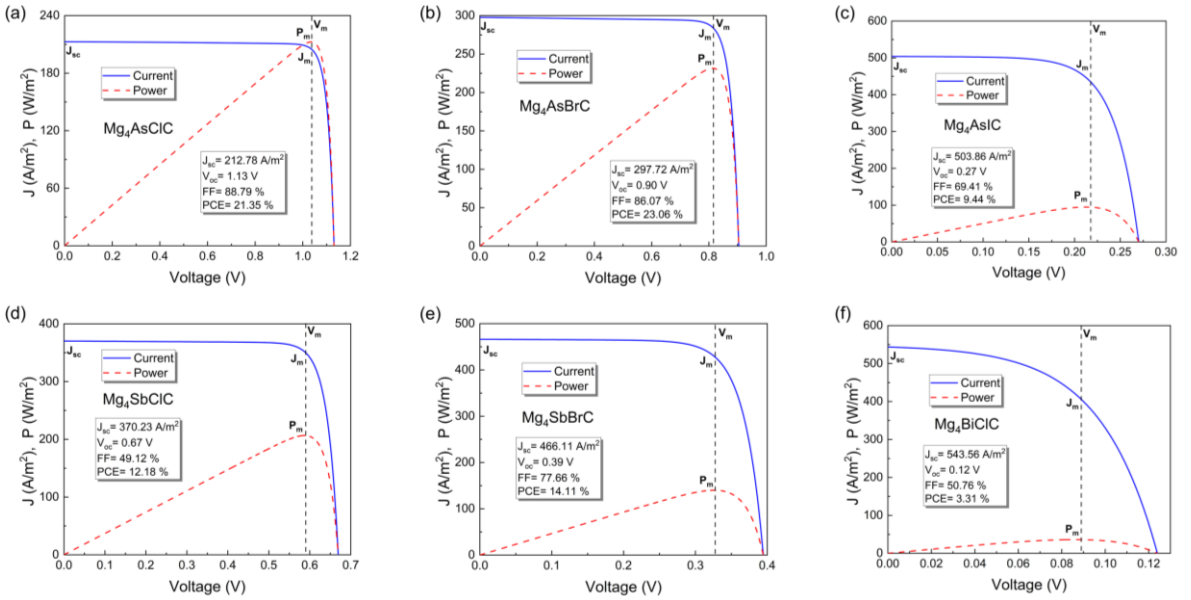

Fig.S17 The *J-V* characteristic curve of $Mg_4AA'C$ simulated using Sentaurus TCAD.

References:

1 M. Sendner, P. K. Nayak, D. A. Egger, S. Beck, C. Müller, B. Epding, W. Kowalsky, L. Kronik, H. J. Snaith, A. pucci, R. Lovrinčić, Optical phonons in methylammonium lead halide perovskites and implications for charge transport, *Mater. Horiz.*, 2016, **3**, 613-620, DOI: 10.1039/C6MH00275G.

2 M. Gajdoš, K. Hummer, G. Kresse, J. Furthmüller, F. Bechstedt, Linear optical properties in the projector-augmented wave methodology, *Phys. Rev. B*, 2006, **73**, 045112, DOI: 10.1103/PhysRevB.73.045112.

3 B. Pal, A. J. Kale, M. Sharma, K. C. Bhamu, S. G. Kang, V. K. Singh, A. Dixit, Inorganic Cs_2TeX_6 (X = Cl, Br, I) lead-Free vacancy-ordered double-perovskite absorber-based single-junction solar cells with a higher efficiency of ~24%: theoretical insights, *Energy Fuels*, 2024, **38**, 1430-1451, DOI: 10.1021/acs.energyfuels.3c03030.

4 W. Shockley, H. J. Queisser, Detailed balance limit of efficiency of p-n junction solar cells, *J. Appl. Phys.*, 1961, **32**, 510-519, DOI: 10.1063/1.1736034.

5 L. Yu, A. Zunger, Identification of potential photovoltaic absorbers based on first-principles Spectroscopic screening of materials, *Phys. Rev. Lett.*, 2012, **108**, 068701, DOI: 10.1103/PhysRevLett.108.068701.

6 L. Yu, R.S. Kokenyesi, D.A. Keszler, A. Zunger, Inverse design of high absorption thin-film photovoltaic materials, *Adv. Energy Mater.*, 2013, **3**, 43, DOI: 10.1002/aenm.201200538.